Chinese Chemical Letters 33 (2022) 2259–2269

Contents lists available at ScienceDirect

Chinese Chemical Letters

journal homepage: www.elsevier.com/locate/cclet

Recent progress in advanced core-shell metal-based catalysts for electrochemical carbon dioxide reduction

Fengqi Wang[a], Wenlong Zhang[a], Hongbin Wan[b], Chenxi Li[c], Wankai An[a], Xia Sheng[a], Xiaoyu Liang[a], Xiaopeng Wang[a,*], Yunlai Ren[a], Xin Zheng[a], Dongcan Lv[a], Yuchen Qin[a,*]

[a] *College of Sciences, Henan Agricultural University, Zhengzhou 450000, China*
[b] *Oilfield Technology Research Institute of Fengcheng Oilfield Operation Area, Xinjiang Oilfield Company, Karamay 834000, China*
[c] *College of Life Science, Chongqing Normal University, Chongqing 401331, China*

ARTICLE INFO

Article history:
Received 14 June 2021
Revised 14 July 2021
Accepted 14 August 2021
Available online 19 August 2021

Keywords:
CMCs
Electrochemical CO_2RR
Tandem catalysis
Lattice strain effect
Defect engineering

ABSTRACT

Electrochemical carbon dioxide reduction (CO_2RR) plays an important role in solving the problem of high concentration of CO_2 in the atmosphere and realizing carbon cycle. Core-shell structure has many unique features including tandem catalysis, lattice strain effect, defect engineering, which exhibit great potential in electrocatalysis. In this review, we focus on the advanced core-shell metal-based catalysts (CMCs) for electrochemical CO_2RR. The recent progress of CMCs in electrocatalytic CO_2RR is described as the following aspects: (1) The mechanism of electrochemical CO_2RR and evaluation parameters of electrocatalyst performance, (2) preparation methods of core-shell metal catalysts and core-shell structural advantages and (3) advanced CMCs towards electrochemical CO_2RR. Finally, we make a brief conclusion and propose the opportunities and challenges in the field of electrochemical CO_2RR.

1. Introduction

As the development of industry and society, the consumption of fossil fuels has increased seriously [1–5], resulting in excessive CO_2 emission [6–11]. The concentration of CO_2 has reached 412 ppm in 2020, which is higher than the safe limit of 350 ppm [12–15], leading to a series of environmental problems [16,17]. Therefore, the efficient means of CO_2 conversion have been eagerly desired [18–21]. In recent years, electrochemical carbon dioxide reduction (CO_2RR) has attracted wide attention due to the lower energy consumption and environment friendly processes [22,23]. Metal-based nanostructures are generally employed as catalysts for electrochemical CO_2RR. Although many efforts have been paid, the performance of CO_2 conversion and product selectivity are still unsatisfactory. The chemical stability of CO_2 leads to the high energy needed to activate CO_2 molecule, which is blocking the performance of CO_2 conversion. In addition, a wide variety of reduction products could be achieved owing to the multi-electron transfer mechanism of CO_2RR, resulting in the lower selectivity. Therefore, many researchers focus on the preparation of advanced metal-based catalysts to boost the activity and selectivity of electrocatalytic CO_2RR [24].

Recently, metal-based electrocatalysts with core-shell structure (CMCs) have exhibited great potential in electrochemical CO_2RR. For instances, Wu *et al.* utilized the non-classical epitaxial growth mediated by bromine anions (Br^-) to synthesize Pd@Ag cubes with Faraday efficiency (FE) of carbon monoxide (CO) as high as 85% at −0.8 V *vs.* reversible hydrogen electrode (RHE) in 0.5 mol/L $KHCO_3$, which is much higher than the counterparts of Pd octahedron, Ag nanoparticles and Pd-Ag nanoalloys [25]. Chloroplast-like porous bismuth-based core-shell (CPBC) materials present remarkable $FE_{formate} > 94\%$ with high catalysis durability (> 72 h) [26]. Based on their various structures, CMCs can be divided into solid core-shell structure and heterogeneous hollow structure, among which heterogeneous hollow structure includes yolk-shelled structure (solid inside) and interlayer-hetero hollow multi-shelled structure (hollow inside). The core-shell structure generally has a strong synergistic effect. Moreover, based on the lattice mismatch of the shell atoms and the core atoms, core-shell structure can produce strain effect and interfacial effect, which is beneficial to tune the electronic structure of catalysts and boost the CO_2RR performance. It is well known that metal nanoparticles (NPs) such as Au, Ag and Pd have excellent catalytic activity for electrocatalytic CO_2RR, while these metals are expensive and not suitable for large-scale applications. Fabricating CMCs could reduce the amount of noble metals,

---

* Corresponding authors.
E-mail addresses: xpwang@henau.edu.cn (X. Wang), qinyuchen@henau.edu.cn (Y. Qin).

https://doi.org/10.1016/j.cclet.2021.08.074
1001-8417/

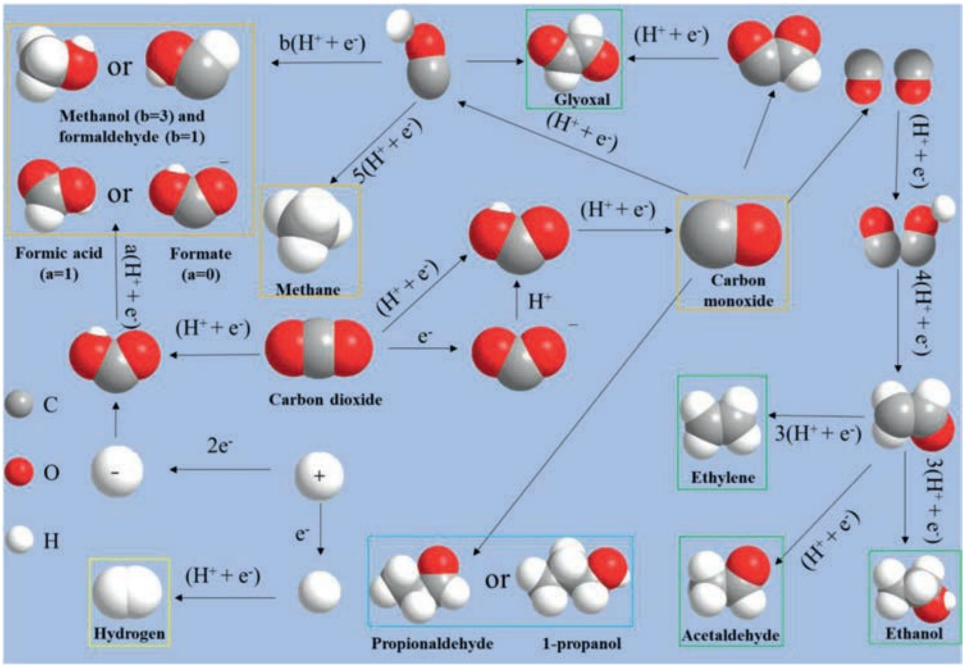

Fig. 1. Reaction mechanism diagram of CO_2 reduction to different products. The gray, red, and white spheres represent C, O, and H atoms, respectively. And the orange box, the green box, the blue box, and the yellow box are C_1 products, C_2 products, C_3 products, and by-products.

which is beneficial to reduce the cost and the large-scale production of catalyst. A stable Au-Fe core-shell nanoparticle (AuFe-CSNP) that is nearly 100 times more reactive to CO_2 reduction than Au NPs at a much lower cost. Additionally, owing to the various combination of core and shell components, CMCs can flexibly integrate many functions and play important roles in the many reactions, including electrochemical reduction of CO_2.

Herein, we summarize the recent developments of CMCs for electrochemical CO_2RR. First, the mechanism and evaluation parameters of electrocatalytic CO_2RR are discussed. Then, the preparation methods and structural advantages of CMCs are evaluated. Based on an in-depth understanding of mechanism and structural advantages, the advanced CMCs for electrochemical CO_2RR are reviewed according to the composition of the core and shell. Finally, a brief summary and several opportunities and challenges are provided for the development of electrochemical CO_2RR.

2. Fundamentals and evaluation parameters of electrochemical CO_2RR

2.1. Mechanism of electrochemical CO_2RR

The C=O bond (750 kJ/mol) is more than twice the energy of the C−C bond (336 kJ/mol) and the C−O bond (327 kJ/mol) [27]. CO_2 is a linear molecule composed of two C=O molecules [28], resulting in the chemically stable. Electrocatalytic CO_2RR involves multi-electron or proton transfer steps, and the whole reaction can be roughly divided into three steps. In the first step, CO_2 molecules are briefly attached to the catalyst surface and then the atoms interact with each other. The second step is activating CO_2 to $CO_2^{\cdot-}$ by one electron transfer, which is the key process of CO_2 reduction. Then, $CO_2^{\cdot-}$ can be easily attached on the surface of catalysts and undergo further reactions. The formation of chemical bonds between CO_2 molecules and suitable electrocatalysts can stabilize $CO_2^{\cdot-}$ radical or reaction intermediates, which can reduce the negative redox potential and ultimately promote the reduction of CO_2 to other substances. As shown in Fig. 1, $CO_2^{\cdot-}$ could be further reduced to CO or other products through different electron transfer pathways. Excessive accumulation of reduction products on the surface will hinder the adsorption of new CO_2 molecules and affect the continuous process of subsequent reactions. Moreover, when the reduction product is CO, the accumulation of CO on the surface of the catalyst will poison the catalyst and eventually lead to the loss of catalytic activity. Therefore, the third step is desorption of reduction products from the catalysts, which plays an important role in the catalytic stability.

The reduction products generated by electrocatalytic CO_2RR in aqueous solution are different with different electron transfer numbers. Table 1 shows the half electrochemical thermodynamic reactions of the common C_1 and C_{2+} reduction products, their corresponding reduction potentials *vs.* standard hydrogen electrode (SHE) and the number of electrons transferred. The reaction products are closely related to the adsorption strength of CO at the active site of catalyst. When the CO intermediate is weakly adsorbed on the catalyst, it will desorb and become the main reduction product; when it adsorbs strongly on the catalyst (such as Pt or Pd), it will poison the surface of the catalyst. An intermediate strength of adsorption of CO results in the formation of hydrocarbons and oxygenates. The generation of advanced reduction products is generally divided into two steps: CO_2 is electrically reduced to CO, and then the bimolecular CO is electrically reduced to other advanced organic molecules. The occurrence of the second step reaction is closely related to the nature of the catalyst, local pH, electrolyte, temperature, the concentration of CO_2 and CO. The high overpotential associated with adverse thermodynamics and low FE of specific products are the biggest challenges for CO_2RR. The lattice mismatch between core and shell in the CMCs can be used to shift the d-band center of surface elements, leading to affect the adsorption strength of various intermediates. Therefore, core-shell catalysts can be used to improve the FE of specific products by reducing overpotential or creating new reaction pathways. Because of its unique structural composition, CMCs are easier to reduce CO_2 to higher C_{2+} products. In addition, it should be noted that hydrogen evolution reaction (HER) [29–31] generally is regarded as the primary competitive reaction for CO_2 reduction, which seriously affects the performance of CO_2 reduction.

Table 1
Standard hydrogen electrode to convert CO_2 to various C_1 and C_{2+} products at pH 0, 1.0 bar, and 25 °C in aqueous solution.

Half electrochemical thermodynamic reactions	Standard redox potentials (V *vs.* SHE)	Number of electrons transferred
CO_2 (g) + $2H^+$ + $2e^-$ = HCOOH (l)	−0.25	2
CO_2 (g) + $2H^+$ + $2e^-$ = CO (g) + H_2O (l)	−0.117	2
CO_2 (g) + $4H^+$ + $4e^-$ = HCHO (l) + H_2O (l)	−0.067	4
CO_2 (g) + $6H^+$ + $4e^-$ = CH_3OH (l) + H_2O (l)	0.033	4
CO_2 (g) + $8H^+$ + $4e^-$ = CH_4 (g) + $2H_2O$ (l)	0.173	4
$2CO_2$ (g) + $12H^+$ + $12e^-$ = C_2H_4 (g) + $4H_2O$ (l)	0.064	12
$2CO_2$ (g) + $12H^+$ + $12e^-$ = C_2H_5OH (l) + $3H_2O$ (l)	0.084	12
$2CO_2$ (g) + $14H^+$ + $14e^-$ = C_2H_6 (g) + $4H_2O$ (l)	0.143	14
$3CO_2$ (g) + $18H^+$ + $18e^-$ = C_3H_7OH (l) + $5H_2O$ (l)	0.103	18
$2H^+$ + $2e^-$ = H_2 (g)	0.000	2

2.2. Evaluation parameters of performance

In the electrocatalytic CO_2RR, the evaluation parameters of CO_2RR performance are mainly concerned with the following four aspects: FE, current density, turnover number (TON) and turnover frequency (TOF).

FE refers to the ratio of the amount of electric energy transferred to produce a specific product to the total amount of electric energy transferred, which reflects the selectivity to a specific product. The formula for FE is as follows Eqs. 1–3:

$$\mathrm{FE} = \frac{\alpha n_{\mathrm{p}} F}{Q} \tag{1}$$

$$\mathrm{FE}_{\mathrm{gas}} = \frac{\alpha \mathrm{n}_{\mathrm{p}} F}{Q} = \frac{\alpha \times \mathrm{ppm} \times C_{\mathrm{CO_2}} \times t \times F}{22.4Q} \tag{2}$$

$$\mathrm{FE}_{\mathrm{liquid}} = \frac{\alpha n_{\mathrm{i}} F}{Q} = \frac{\alpha \times V_{\mathrm{liquid}} \times \rho_{\mathrm{liquid}} \times F}{M_{\mathrm{liquid}} Q} \tag{3}$$

where α refers to the number of electrons transferred by the reaction, n_p refers to the number of moles of the reduction product, F refers to the Faraday constant, and Q is the total passed charge. FE_{gas} and FE_{liquid} are the FE of gas products and liquid products respectively. ppm is the concentration of the gas products, C_{CO_2} represents the flow rate of CO_2, t is the reaction time, V_{liquid}, ρ_{liquid}, and M_{liquid} refer to the volume, density, and relative molecular weight of the liquid product respectively [32].

Current density refers to the amount of electricity that passes over the catalyst per unit surface area (the electrochemical surface area) per unit time, which reflects the kinetic rate of electrochemical transformation Eq. 4 [33].

$$j_i = i_{total} \times FE_{target} \tag{4}$$

where, j_i is the current density of the target product, j_{total} is the total current density of the reaction, and FE_{target} is the FE of the target product.

The activity of electrocatalyst can be judged by TON and TOF in the field of electrocatalytic CO_2RR, and the calculation formula of the two is as follows Eq. 5 [34]:

$$\mathrm{TON} = \frac{n_{\mathrm{p}}}{n_{\mathrm{c}}}, \mathrm{TOF} = \frac{n_{\mathrm{p}}}{n_{\mathrm{c}} \times t} \tag{5}$$

where n_p is mole of the target product, n_c is moles of catalyst, and t is the reaction time.

2.3. Characterization techniques of CMCs

The structure and components of CMCs are important for their catalytic performance. Therefore, it is necessary to confirm the structure and components of CMCs. Scanning Electron microscopy (SEM) and transmission electron microscopy (TEM) are the most commonly employed means of object structure analysis. SEM is to scan the surface of bulk samples with a focused low-energy electron beam, and then the surface morphology and crystal orientation of the catalyst can be obtained. TEM is to irradiate a thin film sample which can pass through electrons with parallel high-energy electron beam. The electron diffraction pattern of crystal structure information and high-resolution image reflecting the internal structure of the sample can be obtained. Inductively coupled plasma optical emission spectrometer (ICP-OES), X-ray photoelectron spectroscopy (XPS) and Energy dispersive X-ray spectroscopy (EDS) could be used to analyze the composition of samples. ICP-OES, also known as ICP-AES, is an atomic emission spectrometry method using inductively coupled high frequency plasma torch as excitation light source to qualitatively and quantitatively analyze more than 70 metal elements and some non-metal elements in samples. ICP-OES can simultaneously analyze both constant and trace components without complicated two-way observation, which has the advantages of rapidity and wide linear range. XPS tests the valence state and element content of the substance about 10 nanometers on the surface of the object, while EDS cannot measure the valence state and the depth of the test is tens of nanometers to a few microns, so basically it can only make qualitative analysis rather than quantitative analysis of the element content on the surface. X-ray diffraction (XRD) is normally applied to analyze the crystal structure of catalysts. According to the XRD pattern, the sample information, such as amorphous or crystalline, phase composition and crystal cell expansion or contraction, can be obtained.

3. Preparation methods and structural advantages of CMCs

3.1. Synthesis of CMCs

Wet chemical method [35] is the main method for the synthesis of CMCs owing to the simple operation and large-scale production [36]. This preparation method could be divided into one-step [37,38] and multi-step. Up to now, a large number of CMCs have been prepared by wet chemical method and several representative CMCs synthesized through one-step and multi-step methods have been listed in the following Table 2 [32,33,39–61].

3.2. Structural advantages of CMCs

Tandem catalysis: Tandem catalysis refers to two or more continuous catalytic reactions in a reactor that eventually produce the target product, in which the product of the previous step will be the reactant of the next step (Fig. 2) [62,63]. As Le Chatelier's Law [64] shown, the continuous consumption of the products of the previous step will accelerate the reaction rate. There are three essential factors for tandem catalysis. First, different catalytic sites should be arranged in a specific order, that is, the order of each reaction is fixed and cannot be confused or reversed. Second, the

Table 2
Representative CMCs prepared by wet chemical method.

Core@Shell	Metal precursors	Reaction steps	Refs.
Ag@(A-Sn(IV))	AgAc, $SnCl_2$	One step	[32]
Ni-NC@Ni	$Ni(NO_3)·6H_2O$	Three steps	[33]
Ag@Cu	$AgNO_3$, $Cu(OAc)_2·H_2O$	One step	[39]
Cu_2S@Cu-vacancy	$Cu(acetylacetone)_2$	One step	[40]
Au@Pd@Pt	H_2PdCl_4, Au, H_2PtCl_6	One step	[41]
Ag@Co@Ni	$AgNO_3$, $CoCl_2·6H_2O$, $NiCl_2·6H_2O$	One step	[42]
$Au_{94}Pd_6$@Pd	$HAuCl_4$, Na_2PdCl_4	One step	[43]
$Pd_{0.8}Au$@Pd	Na_2PdCl_4, $HAuCl_4$	One step	[44]
Sn-Cu/SnO_x	$SnSO_4$, $CuSO_4$	One step	[45]
PtPb@ PtNi	$Pd(acac)_2$, $Pb(HCOO)_2$	One step	[46]
PtPb@Pt	$Pt(acac)_2$, $Pb(acac)_2$	One step	[47]
AuFe@Au	$Fe(acac)_3$, $Au(OOCCH_3)_3$	One step	[48]
Ag@Au	$AgNO_3$, $HAuCl_4$	Two steps	[49]
Cu@Sn	$CuSO_4·5H_2O$, $SnCl_2·2H_2O$	Two steps	[50]
Ni_2P@Ho_2O_3	$Ni(acac)_2$, $Ho(acac)_3$	Three steps	[51]
Ag@$AgCl_x$	Ag foil	Three steps	[52]
Fe_xN@Fe-N-C	$FeSO_4·7H_2O$	Four steps	[53]
Au@Cu_2O	$HAuCl_4$, $Cu(NO_3)_2$	Two steps	[54]
$AuCu_3$@Au	Cu, Au	Two steps	[55]
AgSn@SnO_x	$AgNO_3$, $Sn(Ac)_2$	Two steps	[56]
Ru@Pt	$RuCl_3$, H_2PtCl_6	Two steps	[57]
Ag@Au	$HAuCl_4$, $AgNO_3$	Two steps	[58]
AuCu@Au	$HAuCl_4·3H_2O$, $Cu(CH_3COO)_2·H_2O$	Two steps	[59]
In-doped Cu@Cu_2O	$CuSO_4$, $In_2(SO_4)_3$	Three steps	[60]
Cu_2O@SnO_2	$CuCl_2·2H_2O$, $SnCl_4$	Two steps	[61]

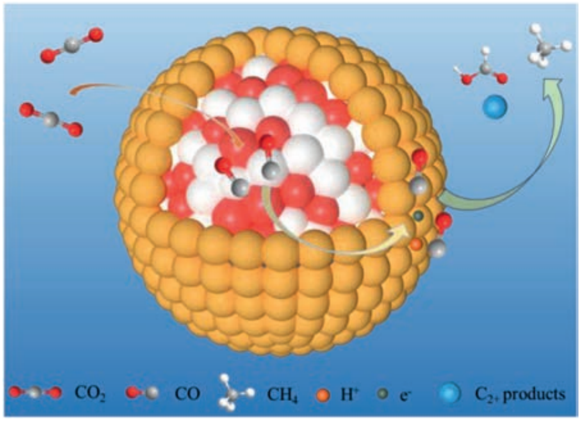

Fig. 2. Schematic diagram of tandem catalysis mechanism of CMCs.

distance between different catalytic sites should be close enough or even direct contact, which is the key to ensure the occurrence of tandem catalysis. Third, the compatibility of different catalytic sites should be considered to prevent these active sites from reacting with each other and interfering with tandem catalysis [65]. The core-shell structure with different inner and outer components is very suitable for multiphase tandem catalysis, especially the interlayer-hetero hollow multi-shelled structure is considered to have great application potential in multiphase tandem catalysis [66]. Besides, CMCs could be employed as an excellent tandem catalyst owing to close distance with unreactive properties of core and shell. These unique structural features well meet the requirements of tandem catalysis. For instance, Zhang *et al.* prepared Au@Cu_2O yolk-shell NPs as tandem catalysts for electrochemical CO_2RR. In this catalyst, CO_2 could be reduced to CO on Au core, and then further reduced to ethanol on the Cu_2O shell, which improves the activity and selectivity of electrochemical CO_2RR to ethanol at a lower electric potential through tandem catalysis [54]. Iyengar *et al.* reported FEs for gaseous and liquid products of Cu-Ag, Cu and Ag catalysts at different potentials in order to demonstrate the role of tandem catalysis in Cu-Ag catalysts [67]. In the range of $-1.1 \sim -1.4$ V_{RHE}, Cu-Ag catalyst has smaller FE_{H2} and FE_{CO} than pure Cu nanocrystals and pure Ag nanocrystals, and gradually becomes smaller with more negative potential, which is related to the tandem catalysis. The efficiency of Cu-Ag catalyst for CO conversion is improved, and the effectiveness of tandem catalysis mechanism is also enhanced.

Lattice strain effect: Lattice strain refers to the deviation from the equilibrium spacing between atoms in the crystal lattice of core shell catalysts [68–71]. The core-shell catalysts may have compression or tensile strain owing to the mismatch between core atoms and shell atoms, which could tune the electronic structure of catalysts and affect the catalytic properties. For example, the binding of *COOH is enhanced on $Au_{60}Pd_{40}$@Pd due to the strain effect between Au and Pd. Therefore, the activation of CO_2 to *COOH is easier to reach 0.10 eV than on pure Pd [43]. Shao *et al.* synthesized twisted $Pd_{0.8}Au$@Pd nanowires (NWs) through a self-assembly strategy. Due to the tensile strain and the ratio of Pd to Au, $Pd_{0.8}Au$@Pd showed superior specific activity and mass activity of CO. The highest selectivity of FE was 94.3% at a relatively low overpotential (−0.6 V) [44].

Interface effect: Compared with traditional mono-component materials, CMCs have special interfaces, and the synergistic effect of these interfaces can improve the catalytic performance of the catalysts. Zhang and his coworkers synthesized core/shell Co_2P/Pt nanorods (NRs) *via* a seed mediated method, and proved that $Co_2P(001)$/Pt(111) interface had the best ORR catalytic performance and $Co_2P(010)$/Pt(111) had the worst ORR catalytic performance by density functional theory (DFT) calculation [72]. Qi *et al.* confirmed that excellent selectivity of Au@CeO_2 CMCs is owing to the interface effect between Au (core) and CeO_2 (shell) [73]. Reasonable use of the interface effect of CMCs is beneficial to the preparation of high-performance catalysts and reduces unnecessary waste at the same time.

Defect engineering: Defects are technically defined as distortions in the periodic structure of the full crystals [74–76]. It can be divided into volume defects and surface defects [77]. According to the previous reports, surface defects such as vacancy and doping could be constructed on CMCs, which are helpful to the enhancement of catalytic properties. Wang and co-workers prepared In-doped Cu@Cu_2O catalyst by co-electrodeposition. The FE of CO reaches to 87.6% ± 2.2%, which is far higher than that of other copper-based catalysts [60]. Sargent and co-workers synthesized Cu_2S@Cu core-shell catalysts by taking advantage of the vacancy defect of the sulfur atom in the core of Cu_2S and the copper atom in the shell to change the C_2 reaction path and improve the FE of the reaction product polyols in the electrocatalytic CO_2RR [40].

Stability: As is well-known, the surface energies of catalysts increase significantly as the decrease of size. Therefore, agglomeration of nanoparticles is easy to occur in electrochemical reactions, resulting in the rapid loss of active sites. Fabricating catalysts with core-shell structure could be an effective method to prevent the agglomeration and improve the stability of catalysts. In CMCs, the internal active sites can be well protected by shell, which are employed as the physical barrier to hinder the loss and agglomeration of active sites, increasing the catalytic stability. For instance, monolithic nanoporous core-shell structured $AuCu_3$@Au catalysts, of which FE_{CO} was 97.27% at a partial current density of 5.3 mA/cm^2 at −0.6 V *vs.* RHE, were prepared by oxidizing etching $Au_{20}Cu_{80}$ alloy by An and co-workers [78]. The total current density on the catalyst remains about 10 mA/cm^2 even after electrolysis at −0.7 V for 100 h, indicating the $AuCu_3$@Au catalysts are very stable. Zhang *et al.* synthesized Cu_2O-SnO_2 core-shell electrocatalysts with shell thickness of 5 nm by adjusting the content of tin precursors. The FE_{CO} is more than 90% at a low overpotential of 390 mV. The catalyst showed superior stability over 18 h at −0.6 V *vs.* RHE in 0.5 mol/L $KHCO_3$ electrolyte [61].

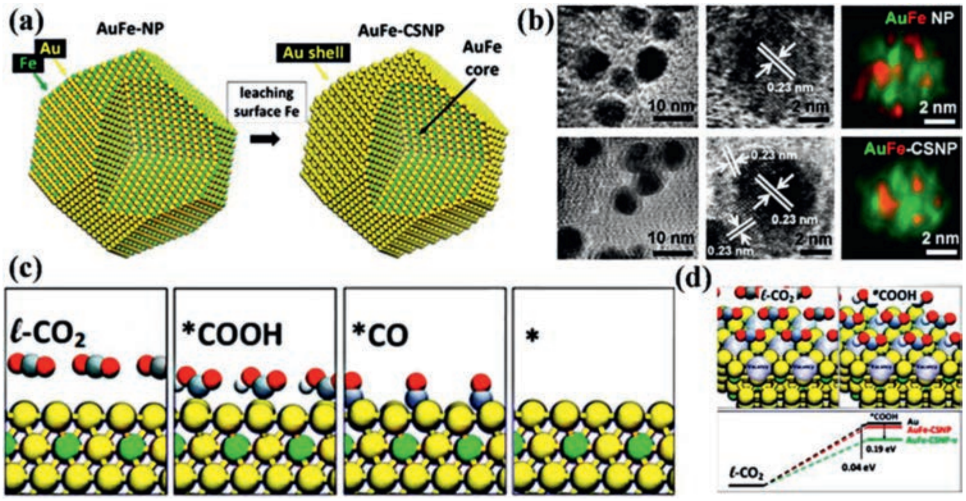

Fig. 3. (a) Schematic synthesis diagram of AuFe-CSNP. (b) TEM and HRTEM images and element map of AuFe-NPs and AuFe-CSNP, respectively. The green part is Au and the red part is Fe in the element map. (c) The CO_2RR reaction steps on Au-M binary alloys include the physical adsorption of CO_2, *COOH, *CO and *(* stands for surface site). The yellow, green, silver, red, and white balls represent Au, M, C, O, and H, respectively. (d) l-CO_2 and *COOH are on the surface with vacancies. Formation energy diagram of *COOH generated by Au, AuFe-CSNP and AuFe-CSNP with vacancies (AuFe-CSNP-v) in CO_2RR. Reproduced with permission [48]. Copyright 2017, American Chemical Society.

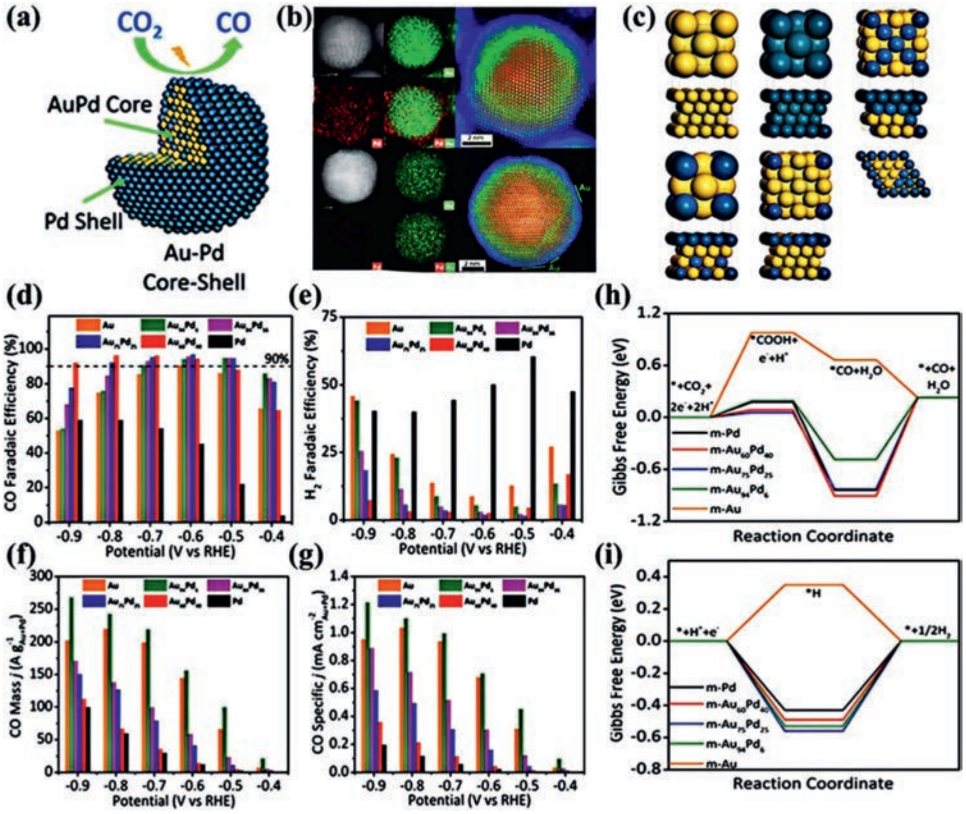

Fig. 4. (a) Schematic illustration of CO_2RR mechanism in the Au-Pd core-shell structure. (b) $Au_{60}Pd_{40}$ NPs of STEM-HAADF, XEDS element mapping and HAADF images. $Au_{94}Pd_6$ NPs of STEM-HAADF, XEDS element mapping, and color HAADF images. The green lines represent the Au atoms isolated from the surface of $Au_{94}Pd_6$ NPs. (c) Configurations of m-Au, m-Pd, m-$Au_{60}Pd_{40}$, m-$Au_{75}Pd_{25}$, and m-$Au_{94}Pd_6$ slab models, and the surface element segregation pattern of m-$Au_{94}Pd_6$ from the top view. The images above are the bulk structure, and the images below are the structure after the surface replacement. FE of CO_2 reduction to (d) CO and (e) H_2 on Au, Pd and AuPd alloy catalysts with different contents, and (f) mass and (g) specific activity of Au, Pd and AuPd alloy catalysts with different contents for CO production. Gibbs free energy diagrams of the reaction paths of (h) CO_2RR and (i) HER on different slab model catalysts. Reproduced with permission [43]. Copyright 2019, Royal Society of Chemistry.

4. Performance of electrochemical CO_2RR

CMCs generally exhibit superior catalytic properties of electrochemical CO_2RR due to their unique structural advantages discussed above [79–82]. In this section, the advanced CMCs towards electrochemical CO_2RR are evaluated according to the composition of core and shell.

4.1. Pure metal core-shell structure

Several metal nanostructures such as Au [81–86], Ag [42,58,87] and Pd [41,44,88–90] show excellent catalytic activity of electrocatalytic CO_2RR [91], but the main product is CO. Other metal nanostructures such as Cu, Bi could provide various reduction products [92,93], but the ability of CO_2 conversion is limited. Therefore,

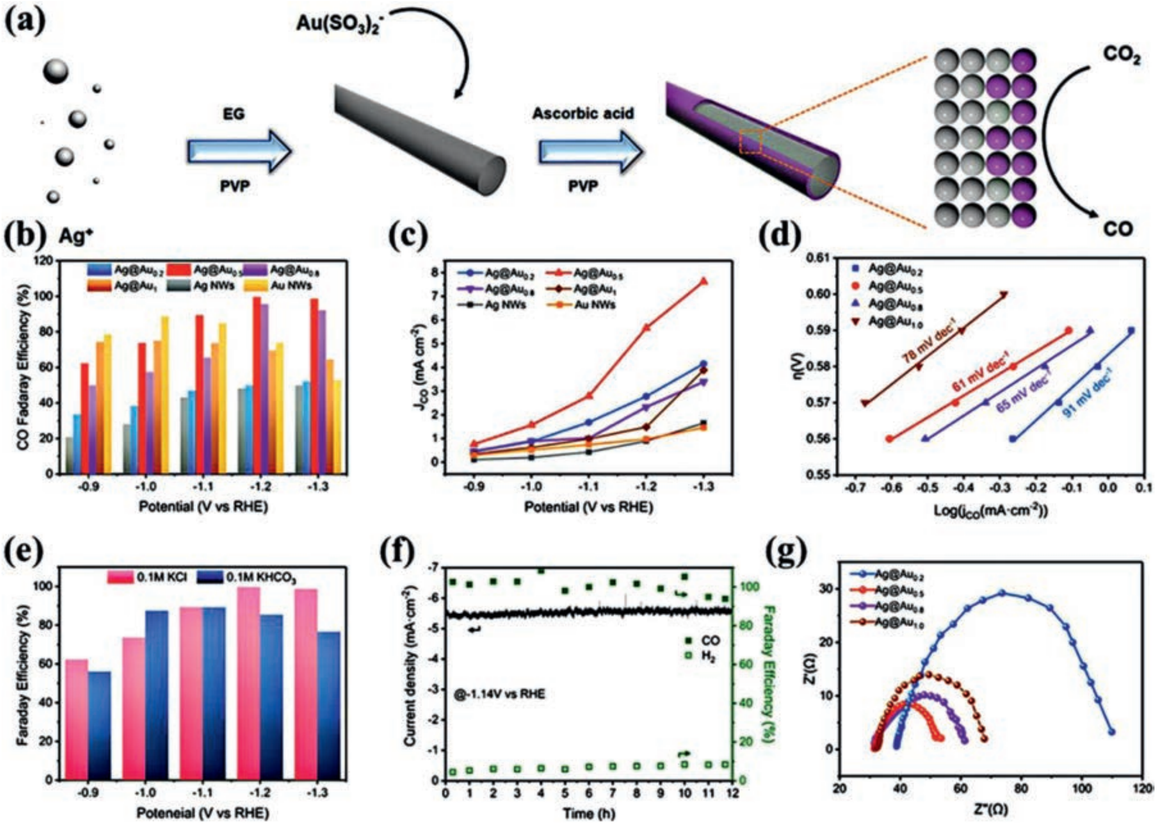

Fig. 5. (a) Schematic diagram of synthesis of Ag@Au NWs. (b) FE_{CO} of different catalysts at different potentials. (c) CO partial current density of different catalysts at different potentials. (d) Tafel slope of different core-shell electrocatalysts. (e) FE_{CO} of $Ag@Au_{0.5}$ electrocatalyst in 0.1 mol/L KCl and 0.1 mol/L $KHCO_3$ solutions. (f) Stability test of $Ag@Au_{0.5}$ catalyst at −1.14 V (*vs.* RHE). (g) electrochemical impedance spectroscopy (EIS) data of different core-shell electrocatalysts. Reproduced with permission [49]. Copyright 2019, Wiley-VCH.

preparing core-shell catalysts with various metals could take the core-shell structural advantages and provide a promising means to enhance the performance of electrochemical CO_2RR [94–103]. Sun *et al.* obtained AuFe-CSNP through leaching out surface Fe of AuFe-CSNP during the electrochemical reduction process (Figs. 3a and b) [48]. Fig. 3c shows the model diagram of the CO_2RR process of Au-mental (M) catalyst. According to the calculation of silico quantum mechanics rapid screening (QM-RS), Au-Fe alloys have a low *COOH formation energy (0.46 eV) and CO desorption energy (0.17 eV). Therefore, Au-Fe alloys are considered to have the potential to improve CO_2 reduction performance. As predicted by the calculation results, AuFe-CSNP exhibits superior mass activity of 48.2 mA/mg towards electrochemical CO_2RR, which is approximate 100 times higher than Au NPs. To estimate the effect of Fe leaching on CO_2RR, Au atom on the surface is further removed to produce Schottky defects. Based on the DFT calculations, the surface defects can reduce the formation of *COOH by 0.19 eV, which confirms that the Schottky defect has a great impact on the catalytic performance of AuFe-CSNPs (Fig. 3d). It demonstrates that the superior activity could be attributed to the defects caused by the surface Fe leaching. Zhu *et al.* prepared AuPd-CSNP by one-pot synthesis method, and the FE_{CO} reached 96.7% at −0.6 V [43]. Through high-angle annular dark field- scanning transmission electron microscopy (HAADF-STEM) and X-ray energy dispersive spectrometry (XEDS) mapping, the element composition and distribution of $Au_{60}Pd_{40}$-CSNP and $Au_{94}Pd_6$-CSNP can be clearly observed (Figs. 4a and b). The atomic model diagrams of m-Au, m-Pd, m-$Au_{60}Pd_{40}$, m-$Au_{75}Pd_{25}$ and m-$Au_{94}Pd_6$ are shown in Fig. 4c. Moreover, it is obvious that when Au:Pd = 94:6, the Pd shell will not be observed by XEDS mapping. In Au, Pd and Au_xPd_{100-x} NPs, the selectivity of CO increases with the increase of Au content (Fig.s 4d-g). The mass activity and specific activity of $Au_{94}Pd_6$-CSNP are higher than other catalysts at −0.9 V to −0.4 V. Figs. 4h and i are the model catalysts with Au:Pd = x:(100 – x), which can be abbreviated as m-Au_xPd_{100-x}. The surface of pure Au has a very high free energy barrier (∼0.98 eV) for the formation of *COOH intermediate, whereas the thermodynamic barrier of pure Pd is much smaller (∼0.18 eV). It can be obtained from Fig. 4h that the activation of CO_2 to *COOH by m-$Au_{60}Pd_{40}$ is 0.10 eV easier than that of pure Pd, which is partly because of strain and ligand effect between Au and Pd, and synergistic results of *COOH coordination changes. In addition, Pd and Au will receive electrons after alloying, and then will lead the downshift of d-band center, but the tensile strain will make d-band center upshift. The overall contribution of these two effects makes the d-band center of Pd upshift to the Fermi energy level and enhance the adsorption of *COOH. Therefore, m-$Au_{94}Pd_6$ surface has the highest *COOH free energy among all the bimetallic surfaces and low HER competition (Fig. 4i). Liu *et al.* employed polyol reduction combined with PVP ligand orientation to deposit Au on Ag NWs for the preparation of Ag@Au NWs (Fig. 5a) [49]. As shown in Figs. 5b–d, $Ag@Au_{0.5}$ NWs show the superior catalytic activity and highest FE_{CO} (Fig. 5b). Moreover, $Ag@Au_{0.5}$ NWs have different CO selectivity at various potentials in CO_2-saturated 0.1 mol/L $KHCO_3$ and CO_2-saturated 0.1 mol/L KCl electrolyte (Fig. 5e). CO_2-saturated 0.1 mol/L $KHCO_3$ as a buffer solution can maintain a neutral environment, while the pH of CO_2-saturated 0.1 mol/L KCl electrolyte will rise as the reaction proceeding, thus inhibiting HER. Additionally, the strong interaction between CO_2 and Cl^- improves the ability of CO_2 capture, resulting in the higher catalytic performance of $Ag@Au_{0.5}$ NWs in 0.1 mol/L KCl solution (Figs. 5f and g).

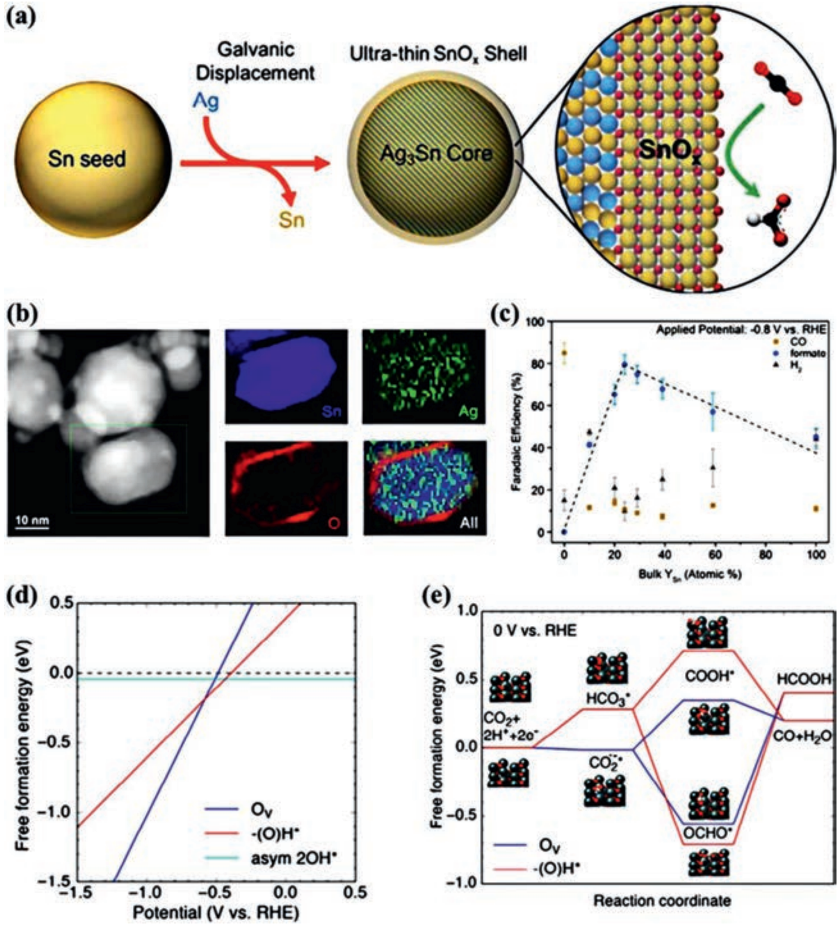

Fig. 6. (a) Synthesis diagram of Ag_3Sn/SnO_x core-shell structure. (b) HAADF-STEM image and electron energy-loss spectroscopy (EELS) of $Ag_{76}Sn_{24}/SnO_x$ catalyst. (c) FE diagram of CO_2 reduction products catalyzed by AgSn /SnO_x catalysts at different concentrations of Sn. (d) The free formation energies of oxygen vacancy (O_v), hydroxyl from H^+ reduction (-(O)H*), and asymmetric hydroxyls (asym 2OH*) from chemical water dissociation on the SnO as a function of potentials *vs.* RHE. (e) The advantageous free energy pathways for CO_2 reduction to CO and HCOOH on SnO. Reproduced with permission [109]. Copyright 2017, American Chemical Society.

4.2. Core-shell structure of metal and metal oxide

Recently, metal and metal oxide heterostructures [104,105] exhibit great potential in electrochemical CO_2RR owing to the interface effect and tandem catalysis [94,106–108]. Fabricating metal and metal oxide catalysts with core-shell structure can remarkably enhance the performance of electrochemical CO_2RR. Wesley *et al.* prepared AgSn/SnO_x NPs though galvanic displacement process, which had an Ag-Sn bimetallic core and an ultra-thin partially oxidized SnO_x shell (Figs. 6a and b) [109]. In this catalyst, the Ag-Sn core is responsible for the high electronic conductivity and SnO_x shell can provide an excellent activity of CO_2 conversion. Owing to the unique structure, AgSn/SnO_x shows superior CO_2RR performance. The FE of formate reaches to ~80% and the formate partial current density is ~16 mA/cm^2 at −0.8 V *vs.* RHE. Though investigating a series of Ag-Sn catalysts with various Ag/Sn compositions, a structure-activity relationship between the AgSn/SnO_x core-shell structure and CO_2RR performance is established and found the optimal thickness of SnO_x shell is 1.7 nm (Fig. 6c). Moreover, according to the DFT calculations, the outstanding catalytic performance of AgSn/SnO_x should be attributed to oxygen vacancies on SnO (101) surface, which is favorable for stabilizing OCHO*, the key intermediate for the HCOOH (Figs. 6d and e). Wang *et al.* obtained Cu-SnO_2 catalysts with three different structures and phases by thermal annealing of CuSn core-shell NPs at various conditions [110]. Among them, CuO/hollow SnO_2 heterostructure shows excellent performance of electrochemical CO_2RR (Fig. 7a and b). It can tune the products from CO to HCOOH with a high FE at ~70% by simply tuning the electrolysis potentials. This promising catalytic properties of CuO/hollow SnO_2 heterostructure can be attributed to the abundant Cu/SnO_2 interfaces, which can decrease ΔG for the formation of *COOH species (Fig. 7c). CuSn NPs/C-A has the highest CO selectivity (FE_{CO} = 70.1%) and the highest current density (1.66 mA/cm^2) at the potential of −0.7 V *vs.* RHE, and CuSn NPs/C-A has the highest HCOOH selectivity (FE_{CO} = 71.5%) and the highest current density (12.6 mA/cm^2) at the potential of −1.0 V *vs.* RHE (Fig. 7d). Li *et al.* demonstrated a new strategy to selectively achieve CO_2 reduction products through tuning synergistic effect between Cu and SnO_2 in Cu@SnO_2 [111]. They found that the product was closely related to the thickness of SnO_2. The reduction product is formate when the thickness of SnO_2 is ~1.8 nm, while changes to CO with FE of ~93% as the thickness of SnO_2 decreases to 0.8 nm. Based on the DFT calculations [112,113], the co-existence of the compressive strain and Cu doped on 0.8 nm SnO_2 shell makes the free energy of CO formation lower than that of formate formation, resulting in the favorite production of CO over formate (Fig. 7e). Ye *et al.* fabricated hierarchical $Sn_{2.7}Cu$ core with amorphous SnO_x shell through one-step electrodeposition [45]. During the electrochemical CO_2RR process, SnO_x shell can be *in situ* reconstructed to Sn/SnO_x interface, which is demonstrated by *in situ* extended X-ray absorption fine structure (EXAFS) and structural examinations. According to the theoretical calculations, the *in situ* reconstructed Sn/SnO_x interface plays a crucial role in facilitating

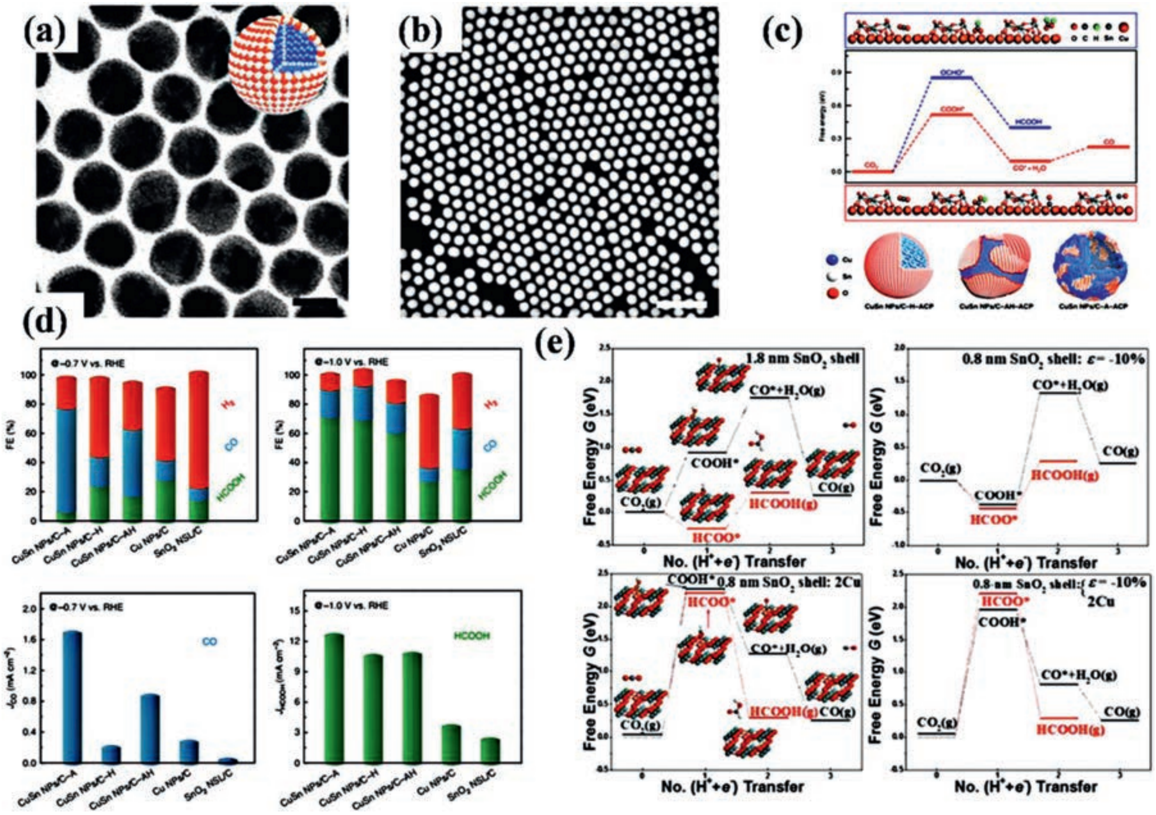

Fig. 7. (a) TEM image, atom model and (b) HAADF-STEM image of CuSn NPs. Scale bars, 20 nm in a, 100 nm in b. (c) Free energy distribution of two paths of CO_2RR over Cu/SnO_2 catalyst. The figures above and below show the geometrical structures of different states (*COOH, OCHO* and *CO) at the Cu/SnO_2 interface. Green, gray, red, reddish-brown, and dark gray spheres represent H, C, O, Cu, and Sn atoms, respectively. (d) FE diagrams of CO, H_2 and HCOOH and current density diagrams of CO and HCOOH for different catalysts at −0.7 V_{RHE} and−1.0 V_{RHE}. Reproduced with permission [110]. Copyright 2018, Springer Nature. (e) The free energy diagrams of the two reaction paths when Cu/SnO_2 catalysts are 1.8 nm-SnO_2 shells, 0.8 nm-SnO_2 shells with 10% uniaxial compression, and 0.8 nm-SnO_2 shells with 2 Cu atoms on the surface and 0.8 nm-SnO_2 shells with 2 Cu atoms on the surface and 10% uniaxial compression. Reproduced with permission [111]. Copyright 2017, American Chemical Society.

formic acid production though optimizing the binding of intermediate HCOO*, resulting in the high FE of C_1 products.

4.3. Core-shell structure of metal-based compounds

In addition to metal oxides, core-shell structures composed of other metal compounds [112–117] also show excellent performance and great application potential in electrocatalytic CO_2RR. Li and co-workers prepared Ag@AgCl_x nanowire arrays by using low-temperature nanoimprinting technique and electrochemical reduction (Figs. 8a and b) [52]. The Ag@AgCl_x nanowire arrays have excellent catalytic activity of CO_2RR. The CO current density is up to 5.27 mA/cm^2 at −0.6 V *vs.* RHE, which is mainly attributed to the strong electron coupling between AgCl_x shell and Ag core and superior CO_2 activation capacity of AgCl_x shells. Fig. 8c shows the change of free energy when CO_2RR occurs on (111) and (211) surfaces of crystalline silver chloride, and Cl modified Ag (111) [Ag(111)_Cl] and (211) surfaces [Ag(211)_Cl], which can indirectly reveal the reason that determines the superior catalytic activity of AgCl_x shell. It can be concluded that Ag (111)_Cl and Ag(211)_Cl are more conducive to the adsorption of *COOH. In addition, Ag on the surface is low coordination, which is easier to combine with *COOH. Cheng *et al.* designed a Fe-N-C nanofiber (Fe-N/CNF), which is a core-shell structure composed of the iron nitride (Fe_xN) NPs encapsulated by Fe and N co-doped carbon layers (Fe_xN@Fe-N-C) [53]. The synthetic steps of Fe_xN@Fe-N-C are complex, including electrospinning, carbonization, acid leaching and nitriding under NH_3. Among them, the nitriding time could affect the formation of core-shell structure. The nitriding time was selected as 10, 20 and 40 min, denoted as Fe-N/CNF-*x* (x = 1, 2 and 4). Fe-N/CNF-2 has excellent catalytic performance (Fig. 8d), the current density has been maintained at value of about 4.5 ± 0.4 mA/cm^2, FE_{CO} fluctuates around 94%. The excellent performance could be attributed to that iron nitride can promote the intermediate desorption of CO from Fe and N doped shells, thus improving the catalytic performance of CO_2.

Reduction products with high carbon numbers possess higher commercial value than C_1 products, but are also more difficult to obtain [118–126]. Kim *et al.* synthesized crystalline/amorphous (C/A) Ni_2P@Ho_2O_3 core shell NPs (CSNPs) by depositing an amorphous Ho_2O_3 shell on the surface of Ni NPs (Fig. 9a). Fig. 9b shows the element mapping of C/A Ni_2P/Ho_2O_3 CSNPs. And the $FE_{acetone}$ of C/A Ni_2P@ Ho_2O_3 is up to 25.4% [51]. The excellent catalytic performance is mainly attributed to its heterostructure. Deng and co-workers synthesized a sheet-like open nanostructure with Ni nanoparticle wrapped by Ni-N species exposed carbon layer (Ni-NC@Ni) through a low-temperature (450 °C) chemical vapor deposition strategy (Fig. 9c) [33]. Ni-NC@Ni electrocatalyst has many advantages, such as the isolated Ni-N species (~4.23 at%) providing the active site for CO_2RR, the open nanostructure of the sheet enlarging the contact area with the electrolyte/reactants, and the Ni nanoparticle core wrapped in the carbon shell acting as an excellent conductor to enhance electron transport. Therefore, Ni-NC@Ni exhibits superior CO_2RR performance. The FE_{CO} is about 87% at 670 mV and the current density is up to 14.8 mA/cm^2 with a long-term stability of more than 150 h (Fig. 9d). Sargent and co-workers synthesized Cu_2S@Cu-V (V stands for vacancy) NPs (Fig. 10a), which can alter the C_2 reaction pathway by shifting se-

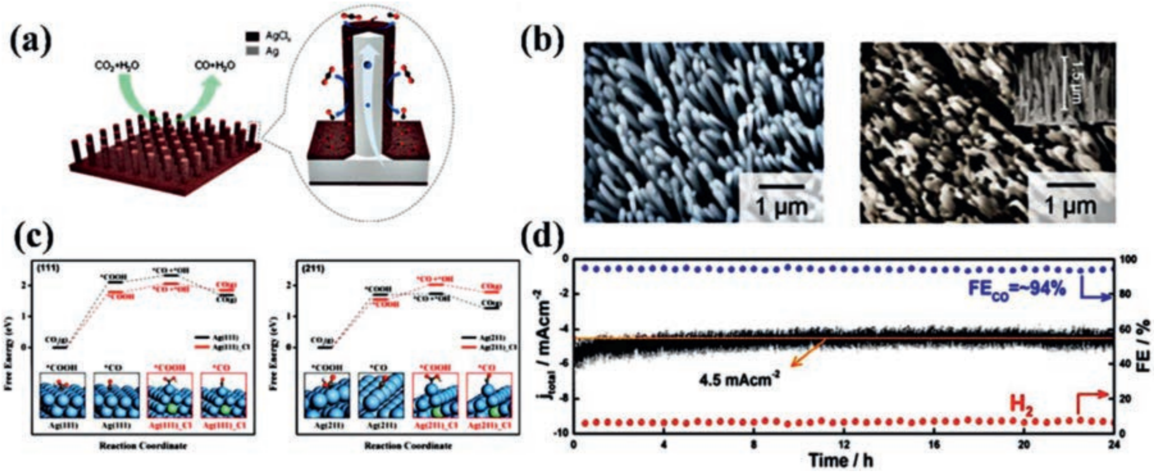

Fig. 8. (a) Schematic diagram of Ag@AgCl$_x$ nanowire array for CO$_2$RR. (b) SEM images of Ag NWs and Ag@AgCl core-shell NWs, the illustration is side view SEM image of the nanowire array. The free energy changes of the CO$_2$RR of (c) Ag (111), Ag (111)_Cl, Ag (211) and Ag (211)_Cl, and the atomic model diagram of the intermediates are shown at the bottom. Ag and Cl are represented by blue and green atoms. Reproduced with permission [52]. Copyright 2019, American Chemical Society. (d) Current density and FE changes of Fe-N/CNF-2 in CO$_2$ reduction at −0.53 V for 24 h. Reproduced with permission [53]. Copyright 2018, American Chemical Society.

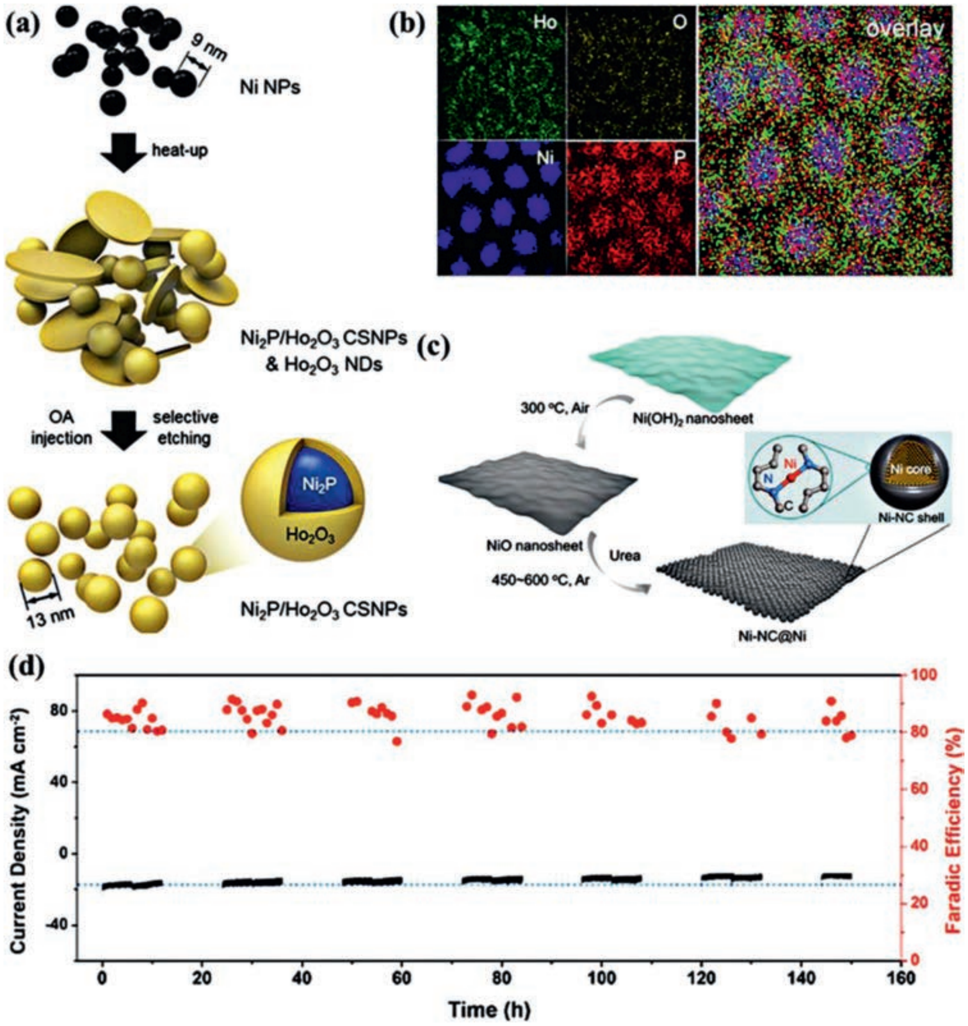

Fig. 9. **(a)** Schematic diagram of synthesis of C/A Ni$_2$P/Ho$_2$O$_3$ CSNPs. OA, NDs stand for oleic acid, nanodisks. (b) Element mapping of each element of C/A Ni$_2$P/Ho$_2$O$_3$ CSNPs. Reproduced with permission [51]. Copyright 2020, American Chemical Society. (c) Schematic formation diagram of Ni-NC@Ni catalyst. (d) Stability of the Ni-NC@Ni for CO$_2$ reduction operated at potentiostatic mode of −0.78 V *vs.* RHE for 150 h with a 0.3 × 0.8 cm^2 working electrode. The black line corresponds to the current density, and the red dot corresponds to the FE. Reproduced with permission [33]. Copyright 2020, Elsevier.

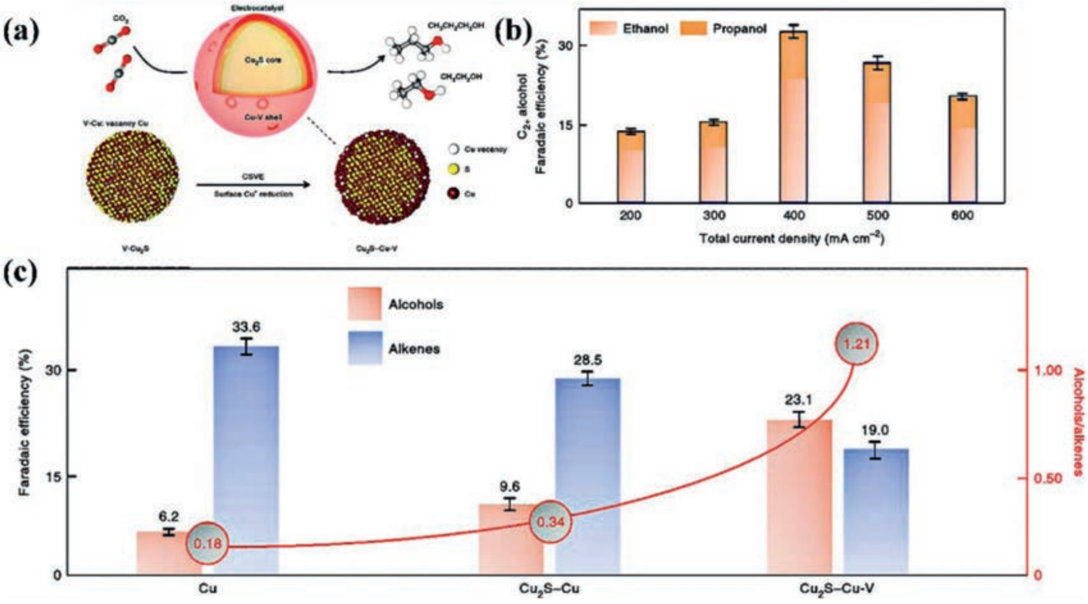

Fig. 10. (a) Schematic diagram of the CO_2RR process occurring on Cu_2S-Cu-V CSVE electrocatalyst. (b) FE of ethanol and propanol over CSVE catalyst at current density of 200–600 mA/cm^2. (c) FE of multi-carbon alcohols and ethylene on different catalysts at −0.95 V *vs.* RHE. Reproduced with permission [40]. Copyright 2018, Springer Nature.

lectivity away from ethylene and towards multi-carbon alcohols [40]. The S atom is introduced to produce vacancy defects on the surface of Cu. This kind of core-shell catalyst with vacancy defects is called core-shell-vacancy engineering (CSVE) catalyst, which can effectively reduce CO_2 to multi-carbon alcohols. Fig. 10b shows the FE of multi-carbon alcohols such as ethanol and propanol catalyzed by CSVE, and Fig. 10c shows the FE of multi-carbon alcohols and ethylene on different catalysts. With the further research on electrocatalytic CO_2RR, more electrocatalyst synthesis methods have been developed.

5. Conclusions and outlook

Global warming and energy crisis have been increasing seriously with the development of industry. Recently, electrochemical CO_2RR provides a promising means for CO_2 recycling and attracts wide attention. In this review, we focus on the advanced metal-based catalysts with core-shell structure towards electrochemical CO_2RR. The preparation methods and structural advantages of CMCs are discussed as well as the mechanism and evaluation parameters of electrochemical CO_2RR. Recent progresses in CMCs for electrocatalytic CO_2RR have been reviewed, with emphasis on the role of core-shell structure played in electrochemical CO_2RR. Although several significant advances have been achieved, the catalytic ability of CMCs for electrochemical CO_2RR is still unsatisfactory. Therefore, several challenges and opportunities are proposed based on our limited knowledge.

Multi-carbon products: Electrocatalytic CO_2RR can reduce CO_2 to a variety of products under mild reaction conditions, such as CO, formaldehyde, methane, ethylene, acetone. However, it is very difficult to obtain high selectivity for a specific product, especially for C_2 and other multi-carbon products. Therefore, improving the selectivity of multi-carbon reduction products is a great challenge of electrochemical reduction of CO_2.

Tandem catalysts: Tandem catalysis is a promising strategy to obtain C_{2+} reduction products of CO_2RR. Various metals have different catalytic properties of electrochemical CO_2RR. For example, Au shows the highest activity of CO_2 reduction due to the weak Au−CO binding energy, but the products are mainly CO. Cu exhibits lower activity, but the products are various including hydrocarbons and oxygenates owing to the intermediate CO binding energy. Therefore, constructing CMCs as tandem catalysts to tune the CO binding energy and reaction process provides a promising means to enhance the activity and selectivity of electrocatalytic CO_2RR.

Phase engineering: Phase structure is one of the most significant structural parameters and has important influences on the catalytic property of catalysts. Especially, the unconventional phases of metal elements generally endow them with wondrous catalytic properties. For instance, Au NPs with 4H phase delivery a higher activity and ethylene selectivity in electrochemical CO_2RR compared to the traditional face center cubic (fcc) Au [127]. Ru NPs with fcc phase also exhibit superior electrocatalytic properties in many reactions than conventional (hexagonal close packed) hcp Ru catalysts [128]. Therefore, fine tuning the phase structure of metals in CMCs exhibits great potential for boosting the performance of electrochemical CO_2RR.

Further reveal the catalytic mechanism: Electrochemical CO_2RR is a complex multi-electron reaction. Through several *in-situ* characterizations to further investigate the electrocatalytic mechanism of CO_2RR plays crucial roles in the enhancement of catalytic properties. *In-situ* synchrotron radiation technologies and *in-situ* HRTEM can be employed to detect the changes in geometric and electronic structure of catalysts. *In-situ* Raman spectra and *in-situ* FT-IR spectra could be used to monitor the changes in the whole CO_2RR process. In general, we believe that more advanced electrocatalysts for CO_2RR could be achieved through a deeper understanding of mechanism and fine-tuning catalyst structure.

Declaration of competing interest

The authors declare that they have no known competing financial interests or personal relationships that could have appeared to influence the work reported in this paper.

Acknowledgments

This research was funded by the National Natural Science Foundation of China (Nos. 21706074 and 21972038), the Natural Science Foundation of Henan Province (No. 2023000410209), the Key Research and Promotion Project of Henan Province (Nos. 202102210261 and 202102310267) and the Top-notch Personnel Fund of Henan Agricultural University (No. 30500682). The Science and Technology Research Program of Chongqing Municipal Education Commission (No. KJQN202000519) and the foundation project of Chongqing Normal University (No. 18XLB008).

References

[1] S. Peh, D. Zhao, Science 369 (2020) 372–373.
[2] N. Wang, R. Miao, G. Lee, et al., Smart Mat. 2 (2021) 12–16.
[3] Y. Qin, H. Zhuo, X. Liang, et al., Dalt. Trans. 48 (2019) 10313–10319.
[4] D. Gao, S. Li, Y. Lv, et al., J. Catal. 376 (2019) 87–100.
[5] M. Wu, Y. Li, X. Liu, et al., Smart Mat. 2 (2021) 5–11.
[6] M. Liu, X. Wang, E.H. Sargent, et al., Joule 3 (2019) 1703–1718.
[7] Z. Wu, F. Gao, M. Gao, Energy Environ. Sci. 14 (2021) 1121–1139.
[8] J.P. Jones, G.K.S. Prakash, G.A. Olah, Isr. J. Chem. 54 (2014) 1451–1466.
[9] D.T. Whipple, P.J.A. Kenis, J. Phys. Chem. Lett. 1 (2010) 3451–3458.
[10] Q. Wang, C. Cai, M. Dai, et al., Small Sci. 1 (2021) 2000028.
[11] Y. Qin, X. Zhang, X. Dai, et al., Small 12 (2016) 524–533.
[12] M. Mikkelsen, M. Jørgensen, F.C. Krebs, Energy Environ. Sci. 3 (2010) 43–81.
[13] N.S. Spinner, J.A. Vega, W.E. Mustain Catal. Sci. Technol. 2 (2012) 19–28.
[14] C. Li, J. Ciston, M.W. Kanan, Nature 508 (2014) 504–507.
[15] D. Zhu, J. Liu, S. Qiao, Adv. Mater. 28 (2016) 3423–3452.
[16] Y. Wang, H. Su, Y. He, et al., Chem. Rev. 120 (2020) 12217–12314.
[17] Y. Liu, T. Wang, X. Fang, et al., Chin. Chem. Lett. 31 (2020) 2712–2716.
[18] J. Liu, C. Chen, K. Zhang, L. Zhang, Chin. Chem. Lett. 32 (2021) 649–659.
[19] Y. Qin, W. F, X. Wang, et al., Rare Met. 40 (2021) 2354–2368.
[20] Y. Tan, K. Lee, H. Song, J. Oh, Joule 4 (2020) 1104–1120.
[21] Y. Chen, K. Chen, J. Fu, et al., Nano Mater. Sci. 2 (2020) 235–247.
[22] T. Wang, J. Yang, J. Chen, et al., Chin. Chem. Lett. 31 (2020) 1438–1442.
[23] J. Xu, K. Wang, S. Zu, B. Han, Z. Wei, ACS Nano 4 (2010) 5019–5026.
[24] H. Pang, X. Meng, P. Li, et al., ACS Energy Lett. 4 (2019) 1387–1393.
[25] Y. Wu, J. Zeng, Y. Yang, et al., Mater. Chem. Front. 5 (2021) 4327–4333.
[26] Y. Wang, R. Yang, Y. Chen, et al., Sci. Bull. 65 (2020) 1635–1642.
[27] K. Li, B. Peng, T. Peng, ACS Catal. 6 (2016) 7485–7527.
[28] L. Zhang, Z. Zhao, J. Gong, Angew. Chem. Int. Ed. 56 (2017) 11326.
[29] Y. Qin, X. Dai, X. Zhang, et al., J. Mater. Chem. A 4 (2016) 3865–3871.
[30] H. Wang, Z. Xu, Z. Zhang, et al., Nanoscale 12 (2020) 22541–22550.
[31] Y. Qin, X. Zhang, X. Dai, et al., J. Mater. Chem. A 3 (2015) 10671–10676.
[32] J. Zhang, M. Qiao, Y. Li, Q. Shao, X. Huang, ACS Appl. Mater. Interfaces 11 (2019) 39722–39727.
[33] Y. He, Y. Li, J. Zhang, et al., Nano Energy 77 (2020) 105010.
[34] M. Schreier, J. Luo, P. Gao, et al., J. Am. Chem. Soc. 138 (2016) 1938–1946.
[35] Z. Zhang, Y. Liu, B. Chen, et al., Adv. Mater. 28 (2016) 10282–10286.
[36] Q. Shao, P. Wang, S. Liu, X. Huang, J. Mater. Chem. A 7 (2019) 20478–20493.
[37] P. Wang, K. Jiang, G. Wang, J. Yao, X. Huang, Angew. Chem. Int. Ed. 55 (2016) 12859.
[38] N. Zhang, L. Bu, S. Guo, J. Guo, X. Huang, Nano Lett. 16 (2016) 5037–5043.
[39] Z. Chang, S. Huo, W. Zhang, J. Fang, H. Wang, J. Phys. Chem. C 121 (2017) 11368–11379.
[40] T. Zhuang, Z. Liang, A. Seifitokaldani, et al., Nat. Catal. 1 (2018) 421–428.
[41] L. He, H. Yang, J. Huang, et al., RSC Adv. 9 (2019) 10168–10173.
[42] F. Qiu, G. Liu, L. Li, et al., Chem. Eur. J. 20 (2014) 505–509.
[43] S. Zhu, X. Qin, Q. Wang, et al., J. Mater. Chem. A 7 (2019) 16954–16961.
[44] S. Zhu, Q. Wang, X. Qin, et al., Adv. Energy Mater. 8 (2018) 1802238.
[45] K. Ye, Z. Zhou, J. Shao, et al., Angew. Chem. Int. Ed. 59 (2020) 4814.
[46] L. Bu, Q. Shao, E. Bin, et al., J. Am. Chem. Soc. 139 (2017) 9576–9582.
[47] L. Bu, N. Zhang, S. Guo, et al., Science 354 (2016) 1410–1414.
[48] K. Sun, T. Cheng, L. Wu, et al., J. Am. Chem. Soc. 139 (2017) 15608–15611.
[49] J. Liu, Y. Wang, H. Jiang, et al., Chem. Asian J. 15 (2020) 425.
[50] X. Hou, Y. Cai, D. Zhang, et al., J. Mater. Chem. A 7 (2019) 3197–3205.
[51] M.G. Kim, Y. Choi, E. Park, et al., ACS Appl. Energy Mater. 3 (2020) 11516–11522.
[52] J. Ge, J. Long, Z. Sun, et al., ACS Appl. Energy Mater. 2 (2019) 6163.
[53] Q. Cheng, K. Mao, L. Ma, et al., ACS Energy Lett. 3 (2018) 1205–1211.
[54] B. Zhang, Y. Wang, S. Xu, et al., RSC Adv. 10 (2020) 19192–19198.
[55] X. Ma, Y. Shen, S. Yao, et al., J. Mater. Chem. A 8 (2020) 3344–3350.
[56] W. Luc, C. Collins, S. Wang, et al., J. Am. Chem. Soc. 139 (2017) 1885–1893.
[57] J. Zou, M. Wu, S. Ning, et al., ACS Sustain. Chem. Eng. 7 (2019) 9007–9016.
[58] A.M. Ismail, E. Csapó, C. Janáky, Electrochim. Acta 313 (2019) 171–178.
[59] D. Kim, C. Xie, N. Becknell, et al., J. Am. Chem. Soc. 139 (2017) 8329–8336.
[60] M. Wang, X. Ren, G. Yuan, et al., J. CO$_2$ Util. 37 (2020) 204–212.
[61] S. Zhang, M. Li, B. Hua, et al., ChemCatChem 11 (2019) 4147.
[62] D. Jagadeesan, Appl. Catal. A 511 (2016) 59–77.
[63] Y. Huang, J. Liang, X. Wang, R. Cao, Chem. Soc. Rev. 46 (2017) 126–157.
[64] C. Xie, Z. Niu, D. Kim, M. Li, P. Yang, Chem. Rev. 120 (2020) 1184–1249.
[65] D.E. Fogg, E.N. Santos, Coord. Chem. Rev. 248 (2004) 2365–2379.
[66] Z. Wang, J. Qi, N. Yang, R. Yu, D. Wang, Mater. Chem. Front. 5 (2021) 1126–1139.
[67] P. Iyengar, M.J. Kolb, J.R. Pankhurst, F. Calle-Vallejo, R. Buonsanti, ACS Catal. 11 (2021) 4456–4463.
[68] Z. Xia, S. Guo, Chem. Soc. Rev. 48 (2019) 3265–3278.
[69] Y. Qin, W. Zhang, K. Guo, et al., Adv. Funct. Mater. 30 (2020) 1910107.
[70] Y. Chen, L. Zhuang, J. Lu, Chin. Chem. Lett. 18 (2007) 1301–1304.
[71] Y. Wang, D. Wang, Y. Li, Smart Mat. 2 (2021) 56–75.
[72] C. Liu, Z. Ma, M. Cui, et al., Nano Lett. 18 (2018) 7870–7875.
[73] J. Qi, J. Chen, G. Li, et al., Energy Environ. Sci. 5 (2012) 8937–8941.
[74] C. Xie, D. Yan, W. Chen, et al., Mater. Today 31 (2019) 47–68.
[75] C. Yang, Y. Zhu, J. Liu, et al., Nano Energy 77 (2020) 105126.
[76] M. Xu, M. Wei, Adv. Funct. Mater. 28 (2018) 1802943.
[77] X. Cui, Z. Zhang, Y. Gong, et al., CCS Chem. 2 (2020) 24–30.
[78] X. Ma, Y. Shen, S. Yao, et al., J. Mater. Chem. A 8 (2020) 3344–3350.
[79] H. Dong, C. Liu, Y. Li, D. Jiang, Nanoscale 11 (2019) 11351–11359.
[80] H. Xie, T. Wang, J. Liang, et al., Nano Today 21 (2018) 41–54.
[81] Z. Yin, G.T.R. Palmore, S. Sun, Trends Chem. 1 (2019) 739–750.
[82] J. Ge, Z. Li, X. Hong, Y. Li, Chem. Eur. J. 25 (2019) 5113.
[83] C. Kuo, T. Hua, M. Huang, J. Am. Chem. Soc. 131 (2009) 17871–17878.
[84] K. Chen, X. Zhang, T. Williams, L. Bourgeois, D.R. MacFarlane, Electrochim. Acta 239 (2017) 84–89.
[85] X. Sun, D. Li, S. Guo, W. Zhu, S. Sun, Nanoscale 8 (2016) 2626–2631.
[86] D.R. Kauffman, D.R. Alfonso, D.N. Tafen, et al., J. Phys. Chem. C 122 (2018) 27991–28000.
[87] S. Kunze, P. Grosse, M. Bernal Lopez, et al., Angew. Chem. Int. Ed. 132 (2020) 22856–22863.
[88] L. Wang, Y. Yamauchi, Chem. Mater. 23 (2011) 2457–2465.
[89] C. Zhang, X. Cheng, Z. Guo, Z. Lv, New J. Chem. 43 (2019) 561–563.
[90] Y. Ge, Z. Huang, C. Ling, et al., J. Am. Chem. Soc. 142 (2020) 18971–18980.
[91] Z. Wei, Y. Zhu, J. Liu, et al., Rare Met. 40 (2021) 767–789.
[92] J. Zeng, K. Bejtka, W. Ju, et al., Appl. Catal. B: Environ. 236 (2018) 475–482.
[93] J. Sun, W. Zheng, S. Lyu, et al., Chin. Chem. Lett. 31 (2020) 1415–1421.
[94] L. Shang, X. Lv, H. Shen, Z. Shao, G. Zheng, J. Colloid Interface Sci. 552 (2019) 426–431.
[95] Q. Wang, L. Shang, D. Sun-Waterhouse, T. Zhang, G. Waterhouse, Smart Mat. 2 (2021) 154–175.
[96] Z. Ban, Y.A. Barnakov, F. Li, V.O. Golub, C.J. O'Connor, J. Mater. Chem. 15 (2005) 4660–4662.
[97] M. Li, Z. Zhao, T. Cheng, et al., Science 354 (2016) 1414–1419.
[98] P. Zhang, X. Zhou, Y. Tang, T.K. Sham, Langmuir 21 (2005) 8502–8508.
[99] J. Xu, T. White, P. Li, et al., J. Am. Chem. Soc. 132 (2010) 10398–10406.
[100] J. Xu, X. Cui, N. Liu, Y. Chen, H. Wang, Smart Mat. 2 (2021) 202–212.
[101] S. Back, M.S. Yeom, Y. Jung, ACS Catal. 5 (2015) 5089–5096.
[102] H. Fu, L. Zhang, L. Zheng, et al., J. Mater. Chem. A 7 (2019) 12420–12425.
[103] C. Yuan, H. Li, Y. Jiang, et al., J. Mater. Chem. A 7 (2019) 6894–6900.
[104] T. Gao, A. Kumar, Z. Shang, et al., Chin. Chem. Lett. 30 (2019) 2274–2278.
[105] K.S. Novoselov, O.A. Mishchenko, O.A. Carvalho, A.C. Neto, Nat. Nanotechnol. 14 (2019) 408–419.
[106] J. Wu, Y. Xie, S. Du, et al., Sci. China Mater. 63 (2020) 2314–2324.
[107] Y. Chen, M.W. Kanan, J. Am. Chem. Soc. 134 (2012) 1986–1989.
[108] F. Abild-Pedersen, J. Greeley, F. Studt, et al., Phys. Rev. Lett. 99 (2007) 016105.
[109] W. Luc, C. Collins, S. Wang, et al., J. Am. Chem. Soc. 139 (2017) 1885–1893.
[110] P. Wang, M. Qiao, Q. Shao, et al., Nat. Commun. 9 (2018) 4933.
[111] Q. Li, J. Fu, W. Zhu, et al., J. Am. Chem. Soc. 139 (2017) 4290–4293.
[112] S. Payra, S. Shenoy, C. Chakraborty, K. Tarafder, S. Roy, ACS Appl. Mater. Interfaces 12 (2020) 19402–19414.
[113] W. Yang, Y. Zhu, J. Li, et al., Chin. Chem. Lett. 32 (2021) 286–290.
[114] X. Wang, S. Liu, K. Huang, et al., Chin. Chem. Lett. 21 (2010) 987–990.
[115] H. Yoon, S. Kim, W. Huang, Y. Sohn, Chin. Chem. Lett. 29 (2018) 800–804.
[116] L. Kong, C. Tang, H. Peng, J. Huang, Q. Zhang, Smart Mat. 1 (2020) 1–35.
[117] Q. Cheng, L. Yang, L. Zou, et al., ACS Catal. 7 (2017) 6864–6871.
[118] Y. Pan, R. Lin, Y. Chen, et al., J. Am. Chem. Soc. 140 (2018) 4218–4221.
[119] H. Yang, N. Han, J. Deng, et al., Adv. Energy Mater. 8 (2018) 1801536.
[120] A.P. Periasamy, R. Ravindranath, S.M.S. Kumar, et al., Nanoscale 10 (2018) 11869–11880.
[121] S. Shen, J. He, X. Peng, et al., J. Mater. Chem. A 6 (2018) 18960–18966.
[122] X. Duan, J. Xu, Z. Wei, et al., Adv. Mater. 29 (2017) 1701784.
[123] S. Munir, A.R. Varzeghani, S. Kaya, Sustain. Energy Fuels 2 (2018) 2532–2541.
[124] I. Kasatkin, P. Kurr, B. Kniep, A. Trunschke, R. Schlögl, Angew. Chem. Int. Ed. 46 (2007) 7324–7327.
[125] X. Liu, X. Wang, B. Zhou, et al., Adv. Funct. Mater. 23 (2013) 1256–1264.
[126] J.M. Luther, P.K. Jain, T. Ewers, A.P. Alivisatos, Nat. Mater. 10 (2011) 361–366.
[127] Y. Wang, C. Li, Z. Fan, et al., Nano Lett. 20 (2020) 8074.
[128] M. Zhao, Y. Xia, Nat. Rev. Mater. 5 (2020) 440–459.